

Multiple scattering effects in pulsed radar systems: An intercomparison study

Original

Multiple scattering effects in pulsed radar systems: An intercomparison study / Battaglia, A.; Kobayashi, S.; Tanelli, S.; Simmer, C.; Im, E.. - In: JOURNAL OF ATMOSPHERIC AND OCEANIC TECHNOLOGY. - ISSN 1520-0426. - 25:9(2008), pp. 1556-1567. [10.1175/2008JTECHA1023.1]

Availability:

This version is available at: 11583/2807864 since: 2020-03-31T23:26:53Z

Publisher:

AMER METEOROLOGICAL SOC

Published

DOI:10.1175/2008JTECHA1023.1

Terms of use:

This article is made available under terms and conditions as specified in the corresponding bibliographic description in the repository

Publisher copyright

(Article begins on next page)

Multiple Scattering Effects in Pulsed Radar Systems: An Intercomparison Study

ALESSANDRO BATTAGLIA

Meteorological Institute, University of Bonn, Bonn, Germany

SATORU KOBAYASHI

Applied Materials Inc., Santa Clara, California

SIMONE TANELLI

Jet Propulsion Laboratory, California Institute of Technology, Pasadena, California

CLEMENS SIMMER

Meteorological Institute, University of Bonn, Bonn, Germany

EASTWOOD IM

Jet Propulsion Laboratory, California Institute of Technology, Pasadena, California

(Manuscript received 30 April 2007, in final form 4 October 2007)

ABSTRACT

In this paper, two different numerical methods capable of computing multiple scattering effects in pulsed-radar systems are compared. Both methods are based on the solution of the time-dependent vectorial form of the radiative transfer equation: one exploits the successive order of scattering approximation, the other a forward Monte Carlo technique.

Different benchmark results are presented (including layers of monodisperse spherical water and ice particles), which are of specific interest for W-band spaceborne cloud radars such as CloudSat's or EarthCARE's cloud profiling radars. Results demonstrate a good agreement between the two methods. The pros and cons of the two models are discussed, with a particular focus on the validity of the second order of scattering approximation.

1. Introduction

Past studies (Marzano et al. 2003; Kobayashi et al. 2005, 2007a; Battaglia et al. 2005, 2006b) have shown that multiple scattering (MS) effects may be relevant for high-frequency radar systems in spaceborne configurations (like those planned for the Global Precipitation Mission and EarthCARE or the one currently employed in CloudSat) and for particular hydrometeor scenarios that entail footprints comparable to or larger than the radiation mean free path. MS is linked to at-

tenuation due to scattering and may partly reduce the apparent two-way attenuation. Such an effect is particularly evident in heavy to moderate precipitation, which is not of primary interest for W-band applications; however, even when considering cold-process-produced light rain profiles, its contribution to the overall backscattered power can be nonnegligible (see Battaglia et al. 2007). The retrieval of rain profiles from spaceborne W-band radar measurements presents several challenges that limit the range of applicability to light rain; for example, L'Ecuyer and Stephens (2002) cites 10 mm h^{-1} as an upper limit. Thus, several sources of uncertainty need to be carefully accounted for to minimize systematic biases of the retrievals. Although MS contribution is recognized as one of these, quantitative estimation of such effect for W-band radars has

Corresponding author address: A. Battaglia, Meteorological Institute, University of Bonn, Auf dem Huegel 20, 53121 Bonn, Germany.
E-mail: batta@uni-bonn.de

not yet reached the level of maturity required to include accurate correcting factors into the retrieval schemes—typically developed under the single scattering (SS) approximation—when the MS contribution is large with respect to SS.

In this work, two techniques capable of simulating the MS radar signal are presented: a successive order of scattering approximation and a forward Monte Carlo (fMC)–based approach. In rigor, when considering a finite pulse duration, the operational frequency is no longer monochromatic. However, because a typical bandwidth of cloud profiling radars is on the order of hundreds of kilohertz, this dispersive effect is negligible compared to the operational frequency about 95 GHz. Thus, throughout the paper, the monochromatic treatment will be adopted. In addition to assessing the validity of previous studies, the intercomparison herein provides results that can be used as benchmarks of MS effects for other methods. After a brief introduction to the two methodologies (section 2), the setup of the simulations and the different scenarios are presented, compared, and discussed in section 3. Section 4 discusses deficiencies and strengths of the two models; more details are provided for the assessment of the range of validity of the second order of scattering (SOS) approximation (SOSA) for configurations typical of W-band spaceborne atmospheric radars. Conclusions and remarks appear in section 5.

2. Formalism to evaluate MS effects in radar systems

Figure 1 is a schematic of a layer of hydrometeors of thickness d and a spaceborne radar flying at altitude H_r with a Gaussian antenna pattern with a 3-dB beamwidth θ_d , described by

$$g_n(\theta) = \exp\left(-4 \ln 2 \frac{\theta^2}{\theta_d^2}\right), \quad (1)$$

where θ is the polar zenith angle relative to the antenna axis. The 3-dB footprint radius at the ground is approximated by $L_r \equiv H_r \tan(\theta_d/2)$, and the antenna pattern solid angle Ω_p and the two-way main-lobe solid angle Ω_{2A} are given by

$$\begin{aligned} \Omega_p &\equiv \int g_n(\hat{\Omega}) d\Omega = \frac{\pi\theta_d^2}{4 \ln 2}, \\ \Omega_{2A} &\equiv \int [g_n(\hat{\Omega})]^2 d\Omega = \frac{\pi\theta_d^2}{8 \ln 2}. \end{aligned} \quad (2)$$

The apparent (or effectively measured) received power due to the range gate with range resolution Δr at dis-

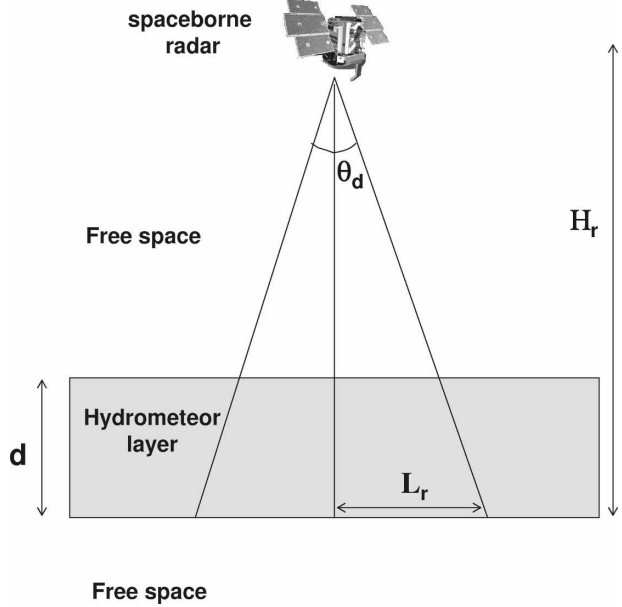


FIG. 1. Schematic for the setup of the simulations. Note that the hydrometeor layer is embedded in free space.

tance r in the presence of MS can be generally expressed as an integral of the received specific intensity from apparent ranges between $r - \Delta r/2$ and $r + \Delta r/2$, $I_a(r, \Delta r, \hat{\Omega})$, weighted by the antenna effective area $A(\hat{\Omega})$ over the solid angle (Marzano and Ferranto 2003); thus,

$$\begin{aligned} \langle P_{aR}(r) \rangle &= \int_{4\pi} A(\hat{\Omega}) I_a(r, \Delta r, \hat{\Omega}) d\Omega, \\ &= A_{e0} \int_{4\pi} g_n(\hat{\Omega}) I_a(r, \Delta r, \hat{\Omega}) d\Omega, \\ &= \frac{\lambda^2}{4\pi} G_0 \int_{4\pi} g_n(\hat{\Omega}) I_a(r, \Delta r, \hat{\Omega}) d\Omega, \end{aligned} \quad (3)$$

where $G_0 = 4\pi / \Omega_p$ and $A_{e0} = \lambda^2 / 4\pi$ are the maximum directive gain and maximum antenna aperture, respectively. The radar equation in the SS approximation is usually written as

$$\begin{aligned} \langle P_{aR}^{[1]}(r) \rangle &= A_{e0} \int_{4\pi} g_n(\hat{\Omega}) I_a^{[1]}(r, \Delta r, \hat{\Omega}) d\Omega, \\ &= \frac{A_{e0} G_0 \Omega_{2A} \Delta r P_T \pi^5 |K|^2}{(4\pi)^2 r^2 \lambda^4} Z^{[1]}(r); \end{aligned} \quad (4)$$

with the SS apparent radar reflectivity. By comparing Eqs. (3) and (4), it is straightforward to introduce an apparent effective reflectivity of order (j) (see details in Battaglia et al. 2006a); that is,

$$Z_e^{(j)} \equiv \left[\frac{\Omega_p \int_{4\pi} g_n(\hat{\Omega}) I_a^{[j]}(r, \Delta r, \hat{\Omega}) r^2 d\Omega}{\Omega_{2A} P_T} \right] \frac{4\pi \lambda^4}{\Delta r \pi^5 |K|^2} \quad (5)$$

associated to the mean value of the apparent received specific intensity for radiation, which has been scattered j times within the medium. Throughout the paper, reflectivities are computed by Eq. (5), with the parameter $|K|^2$ set equal to 0.75 (the standard dielectric factor for liquid water at 94 GHz and 10°C). Equation (5) can be easily generalized to include polarization by substituting the scalar intensity I_a with the Stokes vector \bar{I}_a . Hereafter, particular emphasis is put on the copolar and cross-polar (pedex co and cx , respectively) reflectivities; for instance, $Z_{cx}^{[2]}$ will indicate the fraction of the SOS reflectivity that is cross-polarized with respect to the transmitted signal.

Two numerical models have been recently developed to quantify how MS affects measurements of the radar reflectivity factor and the linear depolarization ratio (LDR) from spaceborne platforms through the computation of elements $Z^{(j)}$ by Eq. (5): a forward Monte Carlo and an SOS method.

a. Forward Monte Carlo

The fMC model is described in detail in Battaglia et al. (2006a). Radiation is launched from the radar with a direction and polarization state resulting from the antenna pattern, and it is traced through the scattering medium by simulating all stochastic processes (e.g., distances traveled before interaction and scattering angles). A biasing technique allows the evaluation of contributions to radar reflectivity at each scattering order [term $I_a^{(j)}$ in (5)], thus allowing for the computation of the total reflectivity Z and the LDR:

$$Z(\text{fMC}) \equiv Z_{co} = \sum_{j=1}^{\infty} Z_{co}^{(j)}, \quad Z_{cx} = \sum_{j=1}^{\infty} Z_{cx}^{(j)}, \quad \text{LDR} \equiv \frac{Z_{cx}}{Z_{co}}. \quad (6)$$

The time dependence is accounted for by gathering radiation that has traveled the same distance within the range resolution (i.e., a rectangular pulse is assumed). The model accounts for general radar configurations (airborne, spaceborne, or ground-based; monostatic or bistatic) and it includes the polarization and the antenna pattern as particularly relevant features. As with all Monte Carlo schemes, the fMC model is very flexible in terms of geometries and definition of scattering medium properties, but it requires significant computational time to achieve high accuracies. This becomes

particularly problematic when dealing with very thick media.

b. Second-order scattering approximation

The second-order scattering approximation for pulsed radar was derived in Kobayashi et al. (2007a), based on the method of Ito et al. (2007). The SOSA approximates the radar return up to the SOS (i.e., $Z(\text{SOSA}) = Z_{co}^1 + Z_{co}^2$). This approximation is obtained as an iterative solution of the time-dependent radiative transfer theory, which also accounts for the transverse and longitudinal shapes of a pulsed beam. Although rectangular pulses are considered here, any pulse shape can be implemented in the model. In this sense, the SOSA is a generalized method of the conventional time-independent radiative transfer theory.

c. Remarks on backscattering enhancement

It is worth mentioning that neither model simulates the effect of backscattering enhancement arising from the cross terms in the Green function method (e.g., de Wolf 1971; Tsang and Ishimaru 1985; Tsang and Kong 2001, 359–405). This effect increases the returned power of multiple scattering by up to roughly 3 dB. Mishchenko (1991, 1992) and Mishchenko et al. (2006) presented compact formulas to calculate the values of cross terms by using the scattering amplitude and Stokes matrix of the corresponding ladder terms. However, note that these formulas can be derived when the right backscattering condition is satisfied. For the spaceborne application of interest here, the assumption of the right backscattering direction cannot be applied, and the degree of departure from the corresponding results depends on the specific geometry as discussed in Kobayashi et al. (2005, 2007b) and is here briefly summarized. The authors studied the moving effect of a satellite, which slightly deviates the scattering angle from the right backscattering condition by 0.0025° , as shown in Fig. 5 in Kobayashi et al. (2005). This small deviation angle has practically no effect on the ladder terms, but it gives finite decorrelations to the corresponding cross terms as illustrated in Kobayashi et al.'s Fig. 5. (Note that in the figure, although the authors plotted the sum of the ladder and cross terms, only the cross terms suffer the decorrelations.) In the same figure, another characteristic of the cross terms, referred to as spatial anisotropy, appears: in the copolarized return rather than in the cross-polarized return, the values of the cross term is represented by a function not only of the backscattering angle but also of the positional relation between the initial polarization and the scattering plane. The spatial anisotropy was first reported

TABLE 1. Outline of the inputs and execution times for the two case scenarios. Computations have been performed on PCs with a 3-GHz Intel processor (fMC) and on a MAC G4 (SOSA). The numbers in parentheses in the last column correspond to the MC realizations used.

| Scenario No. | Frequency (GHz) | Range resolution (m) | H_r (km) | Beamwidth ($^\circ$) | Execution time (min) | |
|--------------|-----------------|----------------------|------------|------------------------|----------------------|------------|
| | | | | | SOSA | fMC |
| I | 95.0 | 100 | 700 | $0.1^\circ, \infty$ | 90/35 | 378 (28 M) |
| II | 95.0 | 100 | 700.5 | 0.1° | 260 | 301 (28 M) |

via experiment and simulation by van Albada and Lagendijk (1987) and van Albada et al. (1987) without mathematical proof as found in appendix A.2 of Kobayashi et al. (2005). Therefore, we have to be careful before simply doubling the value of ladder term without evaluating the biscattering angle and determining the initial polarization direction to the biscattering plane.

The impact of backscattering enhancement is therefore not included in the calculations presented in this paper: in general, such contribution is proportional and not larger than the one given by the ladder terms of order above the first. Further work is necessary to provide accurate estimates of this contribution for the time-dependent, nonexact backscattering scenario considered here.

3. Benchmark results

Two simple benchmark scenarios are considered: the first includes two adjacent layers of ice and rain; the second, three layers, with the intermediate one modeling a melting layer. Below and above the cloud layers, free space is assumed. In all cases, a nadir-looking radar flying at altitude H_r (measured from the bottom of the cloud), as shown in Fig. 1, is considered. An outline of the two simulation inputs is provided in Table 1. The single-layer scenario presented in Kobayashi et al. (2007a) was initially used as a cross-check; the results (not shown) agree quite well in line with the presented case studies.

a. Results for the first scenario

A two-layer scenario including both ice and rain at 95 GHz is considered. The “thin” ice layer is composed of monodisperse ice spheres with a diameter $D = 1$ mm, a concentration of 500.0 m^{-3} , and a refractive index $1.775 + i2.7585 \times 10^{-3}$ located between 4 and 2 km (i.e., the range between 0 to 2 km), with extinction coefficient $k_{\text{ext}} = 0.195 \text{ km}^{-1}$, SS albedo $\omega = 0.983 \text{ 679}$, backscattering coefficient $k_{\text{back}} = 0.1515 \text{ km}^{-1}$, and asymmetry parameter $g = 0.23$. The rain layer is located at ranges between 2 and 4 km and consists of monodisperse water spheres with diameter $D =$

1 mm, concentration 500.0 m^{-3} and refractive index $3.344 \text{ 912} + i \text{ 1.917 564}$ ($k_{\text{ext}} = 1.302 \text{ 182 9 km}^{-1}$, $\omega = 0.510 \text{ 912 6}$, $k_{\text{back}} = 0.758 \text{ 072 km}^{-1}$, and $g = 0.0954$). For ease of reference, the idealized rain layer corresponds approximately to a 4 mm h^{-1} rain rate and would induce a two-way total attenuation of approximately 11 dB in the propagating radar signal. The total optical thickness (i.e., the integral of the extinction coefficient profile) is about 3.

Two antenna patterns are considered: one with $\theta_d = 0.1^\circ$, the other with an infinite aperture (to match the plane wave incidence theory). The range resolution is equal to 100 m. Results for $Z_{\text{co}}^{[1]}$ (the SS copolar signal), $Z_{\text{co}}^{[2]}$ (the SOS copolar signal), and $Z_{\text{cx}}^{[2]}$ (the SOS cross-polar signal), computed both with SOSA and fMC, are shown on the left-hand side of Fig. 2 for both normalized footprints. Because we are dealing with spherical particles, $Z_{\text{cx}}^{[1]}$ (the SS cross-polar signal) is obviously null. All variables are plotted as a function of the range of the leading edge of the radar pulse (with the range equal to zero at the top of the cloud). For instance, the first point inside the cloud evaluated by the fMC corresponds to a 50-m range, which means that half of the radar pulse is within the rain cloud and half is outside of it. This explains why the reflectivity signal is increasing at ranges lower than the range resolution. A similar reasoning explains why the SS signal is not null up to a range equaling 4.1 km (away from the layer bottom located at 4.0 km).

Consistent with Eq. (4), the first order of scattering $Z_{\text{co}}^{[1]}$ is invariant for change in θ_d (note the same pattern in the left-hand side of Fig. 2), with a negative slope dictated by the extinction coefficient (one-way specific attenuation equal to 5.65 and 0.85 dB km^{-1} in the rain and ice layers, respectively) with an obvious transition at the ice–rain border at range = 2 km. On the other hand, the values of $Z_{\text{co}}^{[2]}$ and $Z_{\text{cx}}^{[2]}$ for $\theta_d = 0.1^\circ$ are always lower than those for $\theta_d = \infty$ (cf. the bottom and top left panels in Fig. 2) because of the decreased footprint. The rapid decreases of $Z_{\text{co}}^{[2]}$ and $Z_{\text{cx}}^{[2]}$ (and of Z) for range > 4.0 km where free space is present are due to the same reason.

When considering the same quantities ($Z_{\text{co}}^{[2]}$ and $Z_{\text{co}}^{[2]}$) evaluated with the two methodologies, there are no

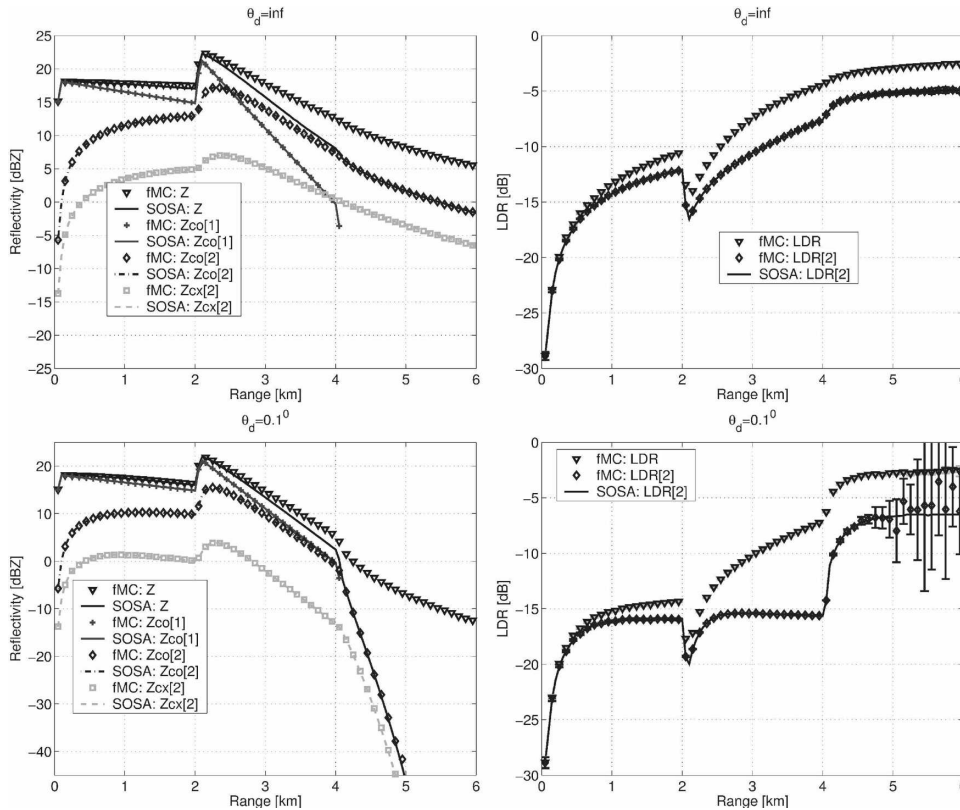


FIG. 2. (left) Reflectivities and (right) linear depolarization ratios vs the range (measured from the top of the hydrometeor layer) for the first scenario (ice layer 0–2 km; rain layer 2–4 km) for (top) an incident plane wave and (bottom) a beamwidth $\theta_d = \text{inf}$, $\theta_d = 0.1^\circ$. Different orders of scattering (see the legend) are plotted.

perceptible differences, at least not at the wide range of scales involved (Fig. 2). Separate plots for the discrepancy between fMC and SOSA [defined as $\Delta Z_{\text{co/cx}}^{[2]} \equiv Z_{\text{co/cx}}^{[2]}(\text{fMC}) - Z_{\text{co/cx}}^{[2]}(\text{SOSA})$] are drawn in Fig. 3. Note that for clarity the two variables have been shifted away from the zero-level baseline. The error bars are representative of the statistical Monte Carlo noise. Note that this error substantially increases when range > 4 km, particularly with $\theta_d = 0.1^\circ$. This is obviously due to the fact that the number of trajectories that contribute to the $Z^{[2]}$ signal decreases considerably for ranges > 4 km (dramatically so when $\theta_d = 0.1^\circ$). This is not a particularly relevant issue because the signal itself is extremely low (e.g., already below -20 dBZ at range = 4.5 km). Within the fMC error and in a region where the signals are not too low (a condition that prejudices the Monte Carlo results), the two solutions agree quite well (better than 0.1 dB). The computational time needed for the results of this simulation are reported in the last column of Table 1. The number of MC realizations used to achieve the errors shown is indicated in parentheses.

On the right-hand side of Fig. 2, the second-order linear depolarization ratio, defined as

$$\text{LDR}[2] \equiv \frac{Z_{\text{cx}}^{[2]}}{Z_{\text{co}}^{[1]} + Z_{\text{co}}^{[2]}} \tag{7}$$

and evaluated using both fMC and SOSA, is shown. The rapid increase in LDR[2] at the rear edge of the rain layer (range = 4 km) is explained by the vanishing of the $Z_{\text{co}}^{[1]}$ contribution at the rear edge of the rain layer. When $\theta_d = \infty$, LDR[2] slowly approaches its second-order asymptotic value. When $\theta_d = 0.1^\circ$ is considered, there is a much faster approach of LDR[2] to the asymptotic value -6.5 dB (for details, see section 3 in Kobayashi et al. 2007a). In fact, the antenna pattern suppression factor makes relevant for the $Z_{\text{cx}}^{[2]}$ and the $Z_{\text{co}}^{[2]}$ signal (at ranges longer than 4 km) only those paths that interact for the first time very close to the rear edge (because this minimizes the departure from the antenna foot) with a scattering angle close to 90° and that are then scattered back to the radar (after traveling horizontally through the medium). Because such paths are only occasionally sampled by the fMC, this also explains the remarkable error bar associated with statistical noise at ranges longer than 5 km, where the co- and cross-polar signals become very low (< -40 dBZ;

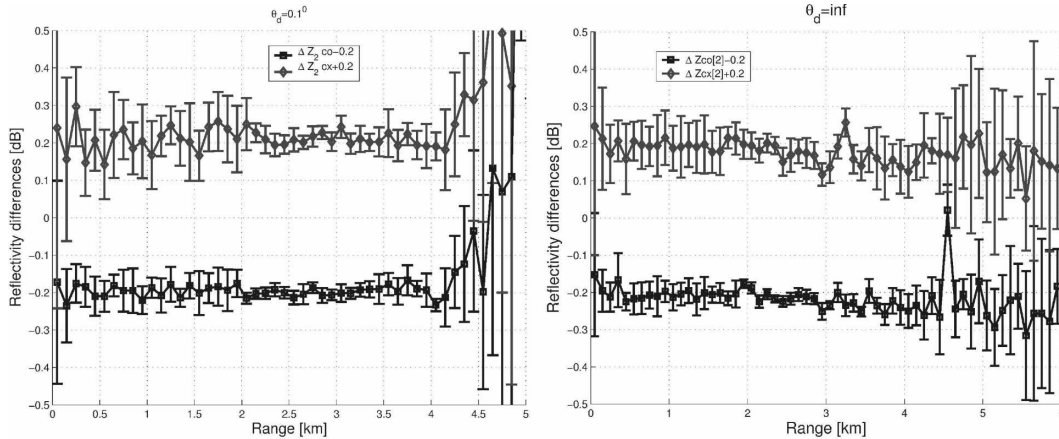


FIG. 3. Relative errors between fMC and SOSA codes for the second-order co- and cross-polar reflectivities [defined as $\Delta Z_{\text{co/cx}}^{[2]} \equiv Z_{\text{co/cx}}^{[2]}(\text{fMC}) - Z_{\text{co/cx}}^{[2]}(\text{SOSA})$], corresponding to the lhs of Fig. 2. The error bars indicate the statistical Monte Carlo noise. For clarity, the two variables have been shifted away from the zero-level baseline.

see bottom right panel in Fig. 2). However, within Monte Carlo noise, LDR[2] values are consistently predicted by the two models.

b. Results for the second scenario

In this case three layers are considered:

- (i) a 2-km layer between 2.5 and 4.5 km composed of monodisperse ice spheres with diameter $D = 1$ mm, concentration 500.0 m^{-3} , and refractive index $1.774\,826 + i2.758\,516 \times 10^{-3}$ ($k_{\text{ext}} = 0.195\,35 \text{ km}^{-1}$, $\varpi = 0.983\,68$, $k_{\text{back}} = 0.151\,49 \text{ km}^{-1}$, and $g = 0.231$);
- (ii) a 0.5-km layer between 2 and 2.5 km composed of monodisperse “melting” ice spheres with diameter $D = 1.2$ mm, concentration 500.0 m^{-3} , and refractive index $1.85 + i2.5 \times 10^{-3}$ ($k_{\text{ext}} = 0.6319 \text{ km}^{-1}$, $\varpi = 0.989\,562$, $k_{\text{back}} = 0.247\,29 \text{ km}^{-1}$, and $g = 0.3873$); and
- (iii) a 2-km rain layer between 0 and 2 km composed of monodisperse water spheres with diameter $D = 0.5$ mm, concentration 500.0 m^{-3} , and refractive index $3.344\,912\,17 + i1.917\,564$ ($k_{\text{ext}} = 0.081\,12 \text{ km}^{-1}$, $\varpi = 0.200\,86$, $k_{\text{back}} = 0.021\,346\,6 \text{ km}^{-1}$, and $g = 0.0575$),

for a total optical thickness equal to 0.87 (i.e., two-way attenuation equals 7.5 dB).

Results are presented in Fig. 4; as before, results of the two codes agree quite well. Note the peculiar pattern of the LDR (center).

4. Discussion

The total copolar reflectivities and LDRs defined by Eq. (6) have been plotted in Figs. 2–4 as reference values (black triangles). In the first scenario, the total sig-

nal is poorly described by both the SS and by the SOSA for ranges longer than 4.0–4.5 km, for which no SS is possible and during which scattering events of order higher than the second are more likely to happen. On the other hand, within the cloud, only in the first case with $\theta_d = +\infty$ (Fig. 2, top left) there is a large discrepancy between the signal computed with all orders of scattering and that evaluated only up to the second order (cf. the triangles and the continuous line).

When looking at the depolarization ratios for both scenarios, LDR[2] departs significantly from LDR. The underestimation is particularly relevant in the second case (Fig. 4, center) for which, in the region between 3.5 and 4.5 km, LDR[2] can underestimate LDR by more than 10 dB. In general, SOSA provides a good estimation of MS effects for cases associated with light rain, whereas fMC accounts for further orders of scattering and hence provides more accurate estimates (with additional computational time required to obtain acceptable uncertainties, with the well-known problem that the accuracy improves proportionally to the square root of the number of realizations). As expected, the SOSA model is faster than the fMC (cf. the last two columns in Table 1). Note, however, that the fMC is set up to solve all orders of scattering and can solve different footprints simultaneously without any additional computational cost. When running it only up to the SOS, the computational times are reduced to 280 and 230 min for the first and second scenarios, respectively.

Although the extremely idealized scenarios analyzed were selected to provide easily reproducible benchmark tests, a more realistic case will be analyzed in this section to provide a more quantitative assessment of the general conclusion reported above. It includes size distributions for frozen and liquid hydrometeors, a sim-

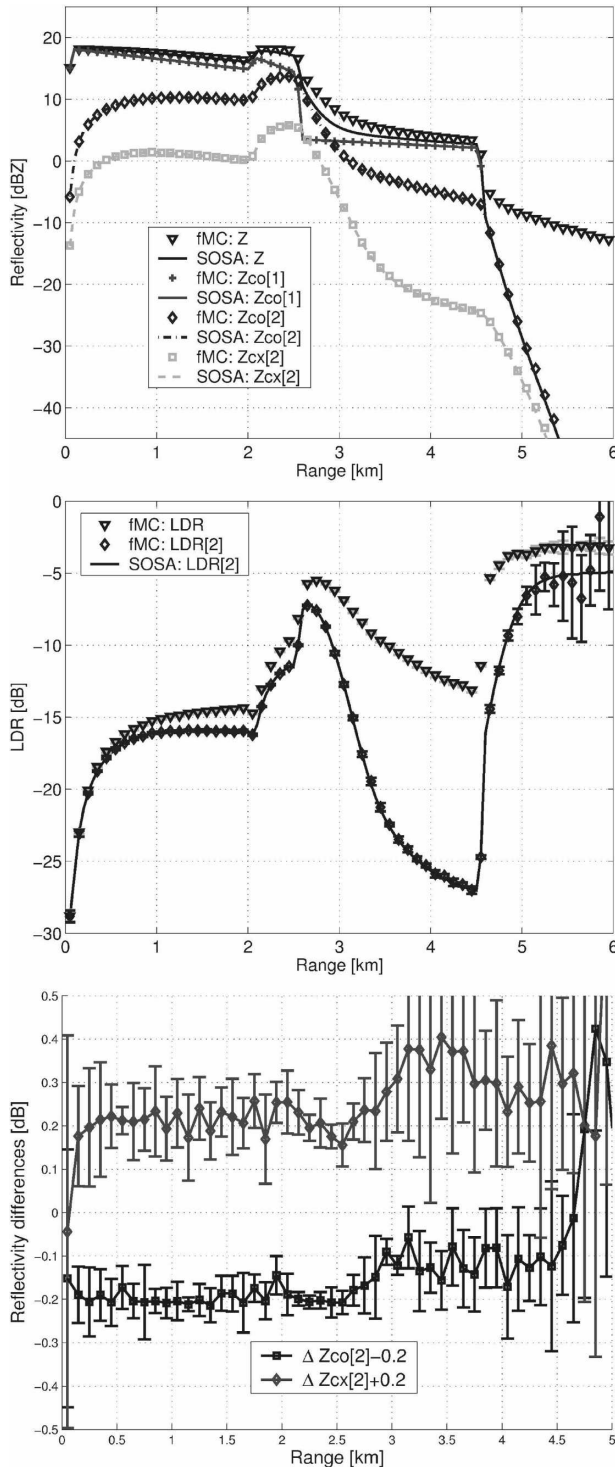


FIG. 4. (top) Reflectivities, (center) linear depolarization ratios, and (bottom) relative errors between fMC and SOSA vs the range within the cloud for the second scenario (three different hydrometeor layers for a total of 4.5 km). Different curves correspond to different scattering orders and different models (see the legend). The radar configuration here employed corresponds to $\theta_d = 0.1^\circ$, $H_r = 700.5$ km.

plified model of melting layer, and the absorption by atmospheric gases.

Importance of higher scattering orders

fMC simulations are used to evaluate the relative importance of orders of scattering higher than two in a configuration typical of W-band spaceborne atmospheric radars (vertical resolution 0.1 km, $\theta_d = 0.1^\circ$, altitude 700 km). Different hydrometeor profiles are considered, including spherical raindrops (between the ground and the freezing level height located at 6 km) and mixed-phase (in the melting layer below 6 km) and ice hydrometeors (above 6 km). As shown in Fig. 5, each profile is characterized by a single parameter, IWC_{fl} (indicated by the filled circle in Fig. 5), the ice water content (IWC) at the freezing level. The size distribution of ice particles is exponential as described in Marshall and Palmer (1948); that is, $N(r) = N_0 e^{-\Lambda_{ice} r}$, where $N_0 = 16 \times 10^3 \text{ m}^{-3} \text{ mm}^{-1}$ and $\Lambda_{ice} = \sqrt{8\pi\rho_{ice} N_0 / IWC}$. The size distribution and rainwater content (RWC) of the rain particles at the bottom of the melting layer (and below) is dictated by a one-to-one correspondence between the ice particles falling across the freezing level and the raindrop into which it melts (i.e., aggregation and break-up processes are neglected). In the melting layer region, the linear behavior of the rain and ice water content is just a naive representation of the simulated process; in fact, each melting particle will be composed of a different fraction of ice, water, and air, depending on its dimension and the altitude below the freezing level. Microphysical parameterizations of falling velocities are extracted from Battaglia et al. (2003). Note that because of the dependence of fall speeds on air density (with higher values at higher altitudes), the rainwater content increases slightly from the bottom of the melting layer to the ground. The ice water content profile decreases linearly with height from the freezing level to the top of the cloud (located at double the freezing level height). Consequently, the mean particle diameter follows a fourth-power curve according to the Marshall–Palmer parameterization adopted here.

Scattering properties are computed according to Mishchenko and Travis (1998). Melting particles are treated as randomly oriented oblate spheroids [with axial ratios according to the quadratic fit of Raynaud et al. (2000), i.e., starting with spherical ice crystals (axial ratio one) and reducing to the axial ratios of oblate-shaped raindrops as defined in Chuang and Beard (1990)], with an effective dielectric constant computed by the Maxwell–Garnett formula with an air matrix with inclusions composed of a water matrix with ice inclusions. This electromagnetic modeling has been

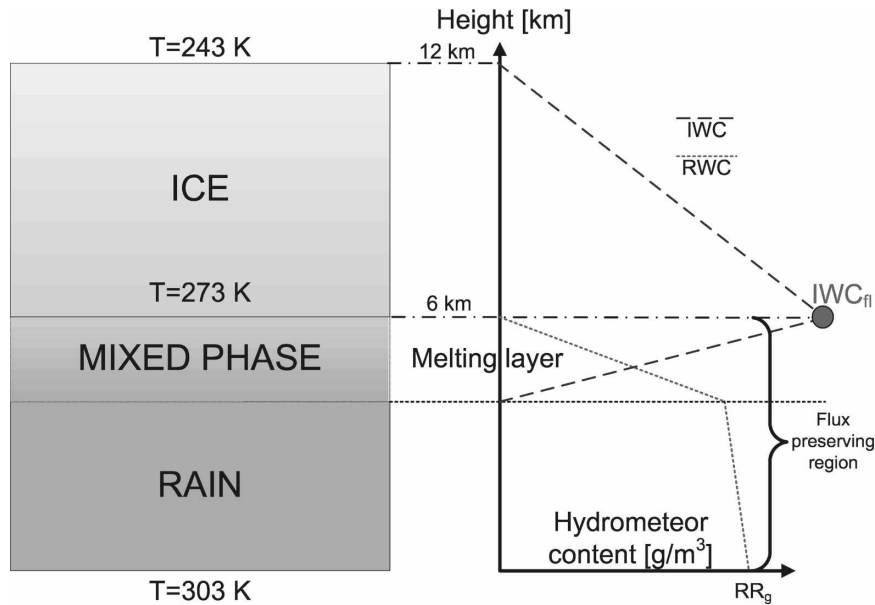


FIG. 5. Schematic for the simulation used in section 4; three different layers are considered. The total RWC and IWC profiles are indicated on the right.

found satisfactory in Battaglia et al. (2003) in fitting Doppler low-frequency radar profiles. Two sets of simulations are performed, with the density of the frozen particles assumed to be 0.1 and 0.6 g cm⁻³ representative and referred to as snow and graupel, respectively. Because of the different densities and parameterizations for falling speeds, the same IWC_{fl} produces different RWC at the ground (and different drop size distribution) for the two sets. For a better discussion, we have classified the profiles according to their rain rate at the ground, indicated with RR_g.

A saturated atmosphere with a constant lapse rate of 5 K km⁻¹ is assumed. Gas absorption is evaluated according to Liebe (1985). A refined vertical resolution of 50 m is used within the melting layer, and resolutions of 1 km and 250 m are adopted within the rain and ice layers, respectively.

Simulations were performed for different values of rain rates RR_g ranging from 0.1 to 20 mm h⁻¹, which correspond to ice contents IWC_{fl} approximately 0.02–3.5 and 0.015–2.0 g m⁻³ for snow and graupel, respectively. Figure 6 shows the cases with RR_g = 2.0 (top) and 10.0 (center) mm h⁻¹. In the reflectivity profiles, the total reflectivity Z (inclusive of all order of scattering), the single scattering reflectivity Z(SS) and the reflectivity contribution in the SOSA Z(SOSA) are drawn together. In the right panels, LDR profiles are plotted: the curve labeled LDR is inclusive of all orders of scattering; the one labeled LDR(SOSA) describes the linear depolarization ratio found by arresting the

expansion to the SOS. Note that LDR(SS) = -∞ above the melting layer (because ice particles are assumed to be spherical) but not below it because raindrops and melting particles are assumed to be oblate particles. Even for RR_g = 2 mm h⁻¹, the SS approximation is unsatisfactory: close to the ground it accounts only for 48% (56% when snowlike densities are considered) of the total reflectivity. On the other hand, 68% (79% for snow) of the signal is accounted for by SOS. The main difference between the snow and graupel profiles is due to the much lower backscattering of the snow particles, which is also responsible for the step in reflectivity at the freezing level altitude. To produce the same 2 mm h⁻¹ amount of rain, IWC_{fl} = 0.38 g m⁻³ of snow (cf. 0.24 g m⁻³ of graupel) is necessary.

When the medium is substantially thicker (optical thicknesses and scattering optical thicknesses are indicated in the graph's titles in Fig. 6), for instance, at RR_g = 10 mm h⁻¹, the impact of MS is clearly more evident. In the lower part of the profile, the signal is completely dominated by higher orders of scattering, with the SOS contribution still an order of magnitude smaller than the actual signal for both density assumptions; however, the MS is significantly higher for the graupel case, which is characterized by a larger total (8.4 versus 6.6) and ice (3.5 versus 1.9) scattering optical thickness. In the case of snow, it is interesting to notice that the SS bright band is replicated in the MS. This is connected to the Maxwell–Garnett approximation, which produces phase functions for snowlike particles

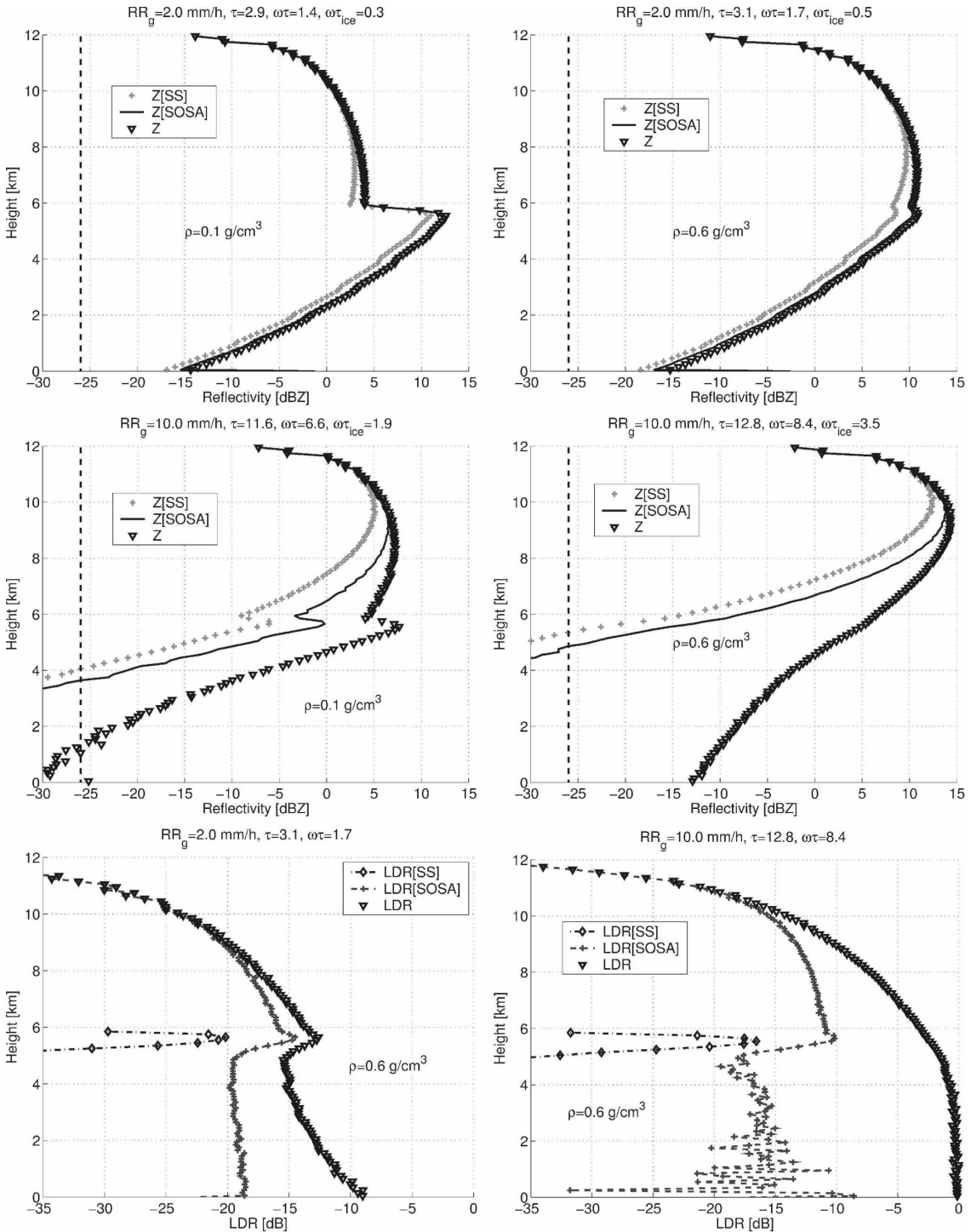


FIG. 6. (top) Scattering reflectivities corresponding to the snow (left) and graupel (right) profiles sketched in Fig. 5; $RR = 2 \text{ mm h}^{-1}$. (center) Same as (top), but for $RR = 10 \text{ mm h}^{-1}$. (bottom): LDR (right) for the graupel profiles shown in the top and central left panels. For clarity, the optical and scattering optical thicknesses of the profiles are included in the panels' titles.

highly peaked in the forward direction (e.g., for the profile analyzed in the central right panel of Fig. 6, the asymmetry parameter is above 0.8 from the freezing level up to 10 km).

In the LDR profiles (bottom of Fig. 6, only shown for the graupel density assumption), the SOS produces results that generally underestimate the entity of depolarization as well; this underestimation generally grows

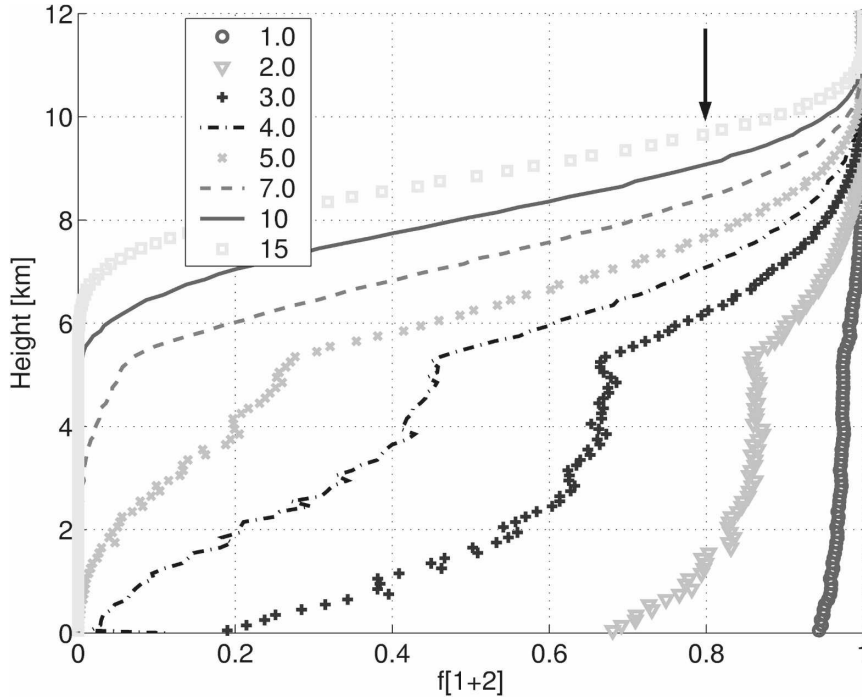


FIG. 7. Degree of approximation of Sosa [as defined in Eq. (8)] for the different hydrometeor profiles illustrated in Fig. 6 corresponding to RR_g (mm h^{-1}). See the legend. A density of 0.6 g cm^{-3} is here assumed for the ice particles.

for longer and longer ranges where it is actually dominated by Monte Carlo noise. Note in particular that LDR comes close to 0 dB at heights near the surface (Fig. 6, bottom right) pointing out the fact that the radiation sensed from that region is more depolarized. This is expected; as the order of scattering increases, differences between copolarization and cross polarization decrease. A confirmation of this behavior can also be found in Fig. 5 of Oguchi and Ihara (2006), where both ladder and cross terms are computed up to seventh order. From our fMC simulations, it seems that in the limit of a very large number of scattering orders (i.e., of high-scattering optical thickness), $LDR \rightarrow 0 \text{ dB}$; proper analytical methods should be developed to check this subtle behavior of MS.

A more comprehensive analysis is depicted in Fig. 7 where the degree of approximation of Sosa, defined as

$$f(\text{SOSA}) \equiv \frac{Z_{\text{co}}^{[1]} + Z_{\text{co}}^{[2]}}{Z_{\text{co}}}, \quad (8)$$

is plotted in linear units. We have arbitrarily selected a value of 80% (equivalent to an error of $\sim 1 \text{ dB}$ and indicated with an arrow in Fig. 7) as a threshold for the Sosa to be applicable (with errors negligible with respect to other sources of error in the measurements) and a value of 50% for the Sosa to be marginally

applicable. These thresholds define two altitudes $H_{80,50\%}(\text{SOSA})$ at which $f_{H_{80,50\%}}(\text{SOSA}) = 80, 50\%$, respectively. When RR_g increases, Sosa becomes unacceptable in wider portions of the profile. A fortiori, things are even worse when SS approximation and the quantities $f(\text{SS}) \equiv Z_{\text{co}}^{[1]}/Z_{\text{co}}$ and $H_{80,50\%}(\text{SS})$ are considered.

The profiles, as defined in Fig. 5, are quite “tall” and are characteristic of deep convection. MS effects are known to be maximized in such conditions (see Battaglia et al. 2006b, 2007). Simulations have been carried out for more typical midlatitude scenarios as well. To mimic such conditions, the profiles of Fig. 5 have been compressed by a factor of 2. The total depth of the system is therefore 6 km, with the freezing level at 3 km (the surface temperature at 288 K) and the mixed layer located between 2 and 3 km. We will refer to these profiles as “shallow.” All results are collected together in Fig. 8, which represents $H_{80,50\%}(\text{SS})$ (dashed–dotted lines) and $H_{80,50\%}(\text{SOSA})$ (continuous lines) as a function of RR_g for the two simulations. Curves with the same symbol and color correspond to profiles indicated in the legend. When increasing RR_g , both $H_{80,50\%}(\text{SS})$ and $H_{80,50\%}(\text{SOSA})$ move to a higher altitude: therefore, SS and Sosa become unsatisfactory in increasingly larger portions of the domain. The distance be-

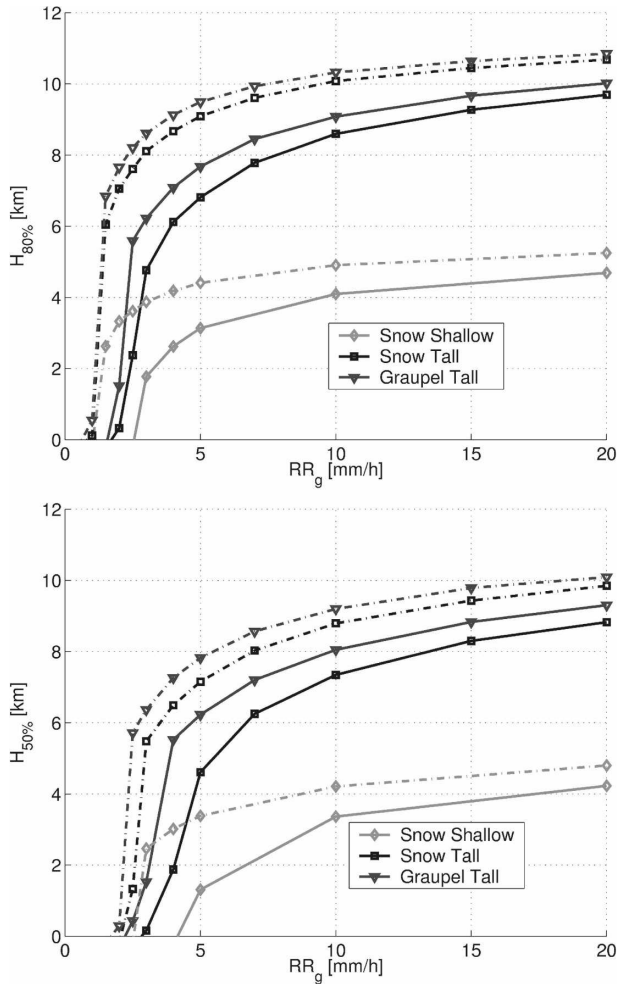


FIG. 8. (top) $H_{80\%}$ and (bottom) $H_{50\%}$ vs RWC_g for different simulations (see the legend). Continuous and dashed-dotted lines correspond to $H(SOSA)$ and $H(SS)$, respectively.

tween lines with the same color and symbols (but different line styles) quantifies the improvement in the reflectivity estimate obtained by the introduction of SOS contributions. As expected, tall systems rich in ice particles produce a large MS effect, versus shallow systems characterized by smaller columnar values of ice content that produce a small effect. Similarly, graupel profiles produce more MS than snow (i.e., soft ice). As a rule of thumb, in our simplistic profiles, for the snow and the graupel cases the SS and SOSA become suboptimal (Fig. 8, top) in the lower part of the domain (close to the surface) for $RR_g > 1.0 \text{ mm h}^{-1}$ and $RR_g > 2.0 \text{ mm h}^{-1}$ for both tall and shallow profiles, respectively. Although the relative impact of MS on the overall received power is dependent on the specific distribution of frozen and liquid hydrometeors, these approximate levels should provide a useful first-order reference in further studies. It is worthwhile to mention

that among the simplifying assumptions made here, absence of cloud liquid water and horizontal homogeneity are assumed. For instance, cloud liquid water contributes to the absorption of the electromagnetic wave in the cloud portion, thereby reducing the overall contribution of MS.

5. Conclusions

Two models capable of treating MS effects in radar systems by solving the time-dependent vector radiative transfer equation have been intercompared. For two simple scenarios involving single or multiple layers composed of either rain or ice or melting particles, results for both co- and cross-polar reflectivities evaluated up to the SOS are quite similar; discrepancies can be attributed to Monte Carlo noise and to small departures introduced by the use of different codes in the computation of the SS parameters. The two scenarios are therefore believed to represent valuable benchmarks, which are useful when validating other radar MS codes. From a computational point of view, the SOSA methodology is very fast and precise, but the Monte Carlo technique is burdened by high computational cost, especially when high accuracies are sought. On the other hand, as currently implemented, the SOSA arrests at the SOS. Although it represents an improvement with respect to the SS modeling, this approximation remains unsatisfactory when dealing with profiles associated with moderate (in our simplified approach, already above 2 mm h^{-1}) and heavy rain, which are likely to be met in real observing systems (like CloudSat). Furthermore, as mentioned in section 2, backscattering enhancement (from cross terms in the analytical scattering theory) is not included in either model, and it should be accounted for as described in Kobayashi et al. (2005, 2007b).

Therefore, our results indicate that it is necessary to include higher-order effects in the analytical theory. This can be realized with the following two methodologies: one is to extend the present second-order formulation directly to the third or higher order, and the other is to combine the second-order theory with a vector diffusion theory. Although the choice between these two depends on the systems of hydrometeors, the latter method seems more promising. An analytical method is worth developing for a systematic study of MS, especially in light of computational time. On the other hand, the fMC allows a great flexibility in terms of the number of layers (with easy extension to 3D scenarios), antenna patterns, and SS properties, with the possibility of introducing dichroic media (i.e., media where the SS properties depend on the direction and polarization) as well.

Moreover, future work should include a systematic analysis of CloudSat data to identify MS-burdened profiles and to improve the correction for MS in the retrieval algorithms.

Acknowledgments. The work by Dr. Satoru Kobayashi, Dr. Simone Tanelli, and Dr. Eastwood Im was performed at the Jet Propulsion Laboratory, California Institute of Technology, under contract with the National Aeronautics and Space Administration. Support from the NASA New Investigator in Earth Science program and from the CloudSat project is gratefully acknowledged. Support and a grant from the TOSCA project funded by the Deutsche Forschungsgemeinschaft are acknowledged as well.

REFERENCES

- Battaglia, A., C. Kummerow, D.-B. Shin, and C. Williams, 2003: Constraining microwave brightness temperatures by radar brightband observations. *J. Atmos. Oceanic Technol.*, **20**, 856–871.
- , M. O. Ajewole, and C. Simmer, 2005: Multiple scattering effects due to hydrometeors on precipitation radar systems. *Geophys. Res. Lett.*, **32**, L19801, doi:10.1029/2005GL023810.
- , —, and —, 2006a: Evaluation of radar multiple scattering effects from a GPM perspective. Part I: Model description and validation. *J. Appl. Meteor. Climatol.*, **45**, 1634–1647.
- , —, and —, 2006b: Evaluation of radar multiple scattering effects from a GPM perspective. Part II: Model results. *J. Appl. Meteor. Climatol.*, **45**, 1648–1664.
- , —, and —, 2007: Evaluation of radar multiple scattering effects in CloudSat configuration. *Atmos. Chem. Phys.*, **7**, 1719–1730.
- Chuang, C., and K. V. Beard, 1990: A numerical model for the equilibrium shape of electrified raindrops. *J. Atmos. Sci.*, **47**, 1374–1389.
- De Wolf, D., 1971: Electromagnetic reflection from an extended turbulent medium: Cumulative forward-scatter single-backscatter approximation. *IEEE Trans. Antennas Propag.*, **19**, 254–262.
- Ito, S., S. Kobayashi, and T. Oguchi, 2007: Multiple-scattering formulation of pulsed beam waves in hydrometeors and its application to millimeter-wave weather radar. *IEEE Geosci. Remote Sens. Lett.*, **4**, 13–17.
- Kobayashi, S., S. Tanelli, and E. Im, 2005: Second-order multiple-scattering theory associated with backscattering enhancement for a millimeter wavelength weather radar with a finite beam width. *Radio Sci.*, **40**, RS6015, doi:10.1029/2004RS003219.
- , S. Ito, S. Tanelli, T. Oguchi, and E. Im, 2007a: A time-dependent multiple scattering theory for a pulsed radar with a finite beam width. *Radio Sci.*, **42**, RS4001, doi:10.1029/2006RS003555.
- , T. Oguchi, S. Tanelli, and E. Im, 2007b: Backscattering enhancement on spheroid-shaped hydrometeors: Considerations in water and ice particles of uniform size, and Marshall–Palmer distributed rains. *Radio Sci.*, **42**, RS2001, doi:10.1029/2006RS003503.
- L’Ecuyer, T. S., and G. L. Stephens, 2002: An estimation-based precipitation retrieval algorithm for attenuating radars. *J. Appl. Meteor.*, **41**, 272–285.
- Liebe, H., 1985: An updated model for millimeter wave propagation in moist air. *Radio Sci.*, **20** (5), 1069–1089.
- Marshall, J. S., and W. M. Palmer, 1948: The distribution of raindrops with size. *J. Meteor.*, **5**, 165–166.
- Marzano, F. S., and G. Ferrauto, 2003: Relation between weather radar equation and first-order backscattering theory. *Atmos. Chem. Phys.*, **3**, 813–821.
- , L. Roberti, S. Di Michele, A. Mugnai, and A. Tassa, 2003: Modeling of apparent radar reflectivity due to convective clouds at attenuating wavelengths. *Radio Sci.*, **38**, 1002, doi:10.1029/2002RS002613.
- Mishchenko, M. I., 1991: Polarization effects in weak localization of light: Calculation of the copolarized and depolarized backscattering enhancement factors. *Phys. Rev. B*, **44** (22), 12 597–12 600.
- , 1992: Enhanced backscattering of polarized light from discrete random media: Calculations in exactly the backscattering direction. *J. Opt. Soc. Amer.*, **9A**, 978–982.
- , and L. D. Travis, 1998: Capabilities and limitations of a current FORTRAN implementation of the T-matrix method for randomly oriented, rotationally symmetric scatterers. *J. Quant. Spectrosc. Radiat. Transfer*, **60**, 309–324.
- , —, and A. A. Lacis, 2006: *Multiple Scattering of Light by Particles: Radiative Transfer and Coherent Backscattering*. Cambridge University Press, 478 pp.
- Oguchi, T., and T. Ihara, 2006: Computer simulation of enhanced backscattering from randomly distributed spherical scatterers at 30 GHz and comparison with measurement. *Radio Sci.*, **41**, RS6002, doi:10.1029/2006RS003468.
- Raynaud, L., I. Chenerie, and J. Lemorton, 2000: Modeling of radiowave scattering in the melting layer of precipitation. *IEEE Trans. Geosci. Remote Sens.*, **38** (4), 1574–1584, doi:10.1109/36.851957.
- Tsang, L., and A. Ishimaru, 1985: Theory of backscattering enhancement of random discrete isotropic scatterers based on the summation of all ladder and cyclical terms. *J. Opt. Soc. Amer.*, **2A**, 1331–1338.
- , and J. A. Kong, 2001: *Scattering of Electromagnetic Waves: Advanced Topics*. Wiley, 413 pp.
- Van Albada, M. P., and A. Lagendijk, 1987: Vector character of light in weak localization: Spatial anisotropy in coherent backscattering from a random medium. *Phys. Rev. B*, **36**, 2353–2356.
- , M. van der Mark, and A. Lagendijk, 1987: Observations of weak localization of light in a finite slab: Anisotropy effects and light path classification. *Phys. Rev. Lett.*, **58**, 361–364.